Comptes Rendus

Physique

Matteo Levantino, Qingyu Kong, Marco Cammarata, Dmitry Khakhulin, Friedrich Schotte, Philip Anfinrud, Victoria Kabanova, Hyotcherl Ihee, Anton Plech, Savo Bratos and Michael Wulff

Structural dynamics probed by X-ray pulses from synchrotrons and XFELs

Physics of ultra-fast phenomena / *Physique des phénomènes ultra-rapides*

Structural dynamics probed by X-ray pulses from synchrotrons and XFELs

Matteo Levantino® [a], **Qingyu Kong**® [b], **Marco Cammarata**® [a],
Dmitry Khakhulin® [c], **Friedrich Schotte**® [d], **Philip Anfinrud**® [d],
Victoria Kabanova® [e], **Hyotcherl Ihee**® [f], **Anton Plech**® [g], **Savo Bratos**® [h]
and Michael Wulff® [*, a]

[a] ESRF — The European Synchrotron, 71 Avenue des Martyrs, 30043 Grenoble Cedex, France

[b] Soleil Synchrotron, L'Orme des Merisiers, 91190 Saint-Aubin, France

[c] European XFEL, 22869 Schenefeld, Germany

[d] National Institute of Health, Bethesda, MD 20892, USA

[e] PSI, SwissFEL, 5232 Villigen, Switzerland

[f] Department of Chemistry, KAIST, Daejeon, South Korea

[g] Karlsruhe Institute of Technology, 76021 Karlsruhe, Germany

[h] Université Pierre et Marie Curie, Paris 75252, France

E-mails: matteo.levantino@esrf.fr (M. Levantino), qingyu.kong@synchrotron-soleil.fr
(Q. Kong), marco.cammarata@esrf.eu (M. Cammarata), dmitry.khakhulin@xfel.eu
(D. Khakhulin), FriedrichS@intra.niddk.nih.gov (F. Schotte),
PhilipA@intra.niddk.nih.gov (P. Anfinrud), victoria.kabanova@gmail.com
(V. Kabanova), hyotcherl.ihee@kaist.ac.kr (H. Ihee), anton.plech@kit.edu (A. Plech),
bratossavo@gmail.com (S. Bratos), wulff@esrf.fr (M. Wulff)

Abstract. This review focuses on how short X-ray pulses from synchrotrons and XFELs can be used to track light-induced structural changes in molecular complexes and proteins via the pump–probe method. The upgrade of the European Synchrotron Radiation Facility to a diffraction-limited storage ring, based on the seven-bend achromat lattice, and how it might boost future pump–probe experiments are described. We discuss some of the first X-ray experiments to achieve 100 ps time resolution, including the dissociation and in-cage recombination of diatomic molecules, as probed by wide-angle X-ray scattering, and the 3D filming of ligand transport in myoglobin, as probed by Laue diffraction. Finally, the use of femtosecond XFEL pulses to investigate primary chemical reactions, bond breakage and bond formation, isomerisation and electron transfer are discussed.

Keywords. Structural dynamics, Synchroton radiation, Pump and probe, Single shot X-ray experiment, Photolysis, Dissociation dynamics.

Available online 13th September 2021

---

* Corresponding author.

1. Introduction

In order to gain a deeper understanding into how physical, chemical and biological processes work at the atomic level, it is important to know how the structure evolves as a function of time. Whereas static structures can often be determined with laboratory X-ray sources, structural characterization of short-lived intermediates requires short, high-intensity X-ray pulses from synchrotrons or Free Electron Lasers (XFEL). Examples of the time and length scales that have been studied with short X-ray and laser pulses are shown in Figure 1. These processes span 18 orders of magnitude in time, from attoseconds to seconds. The time scale of a given process is intimately linked to the length scale. For example, conformational changes in proteins evolve on the microsecond to millisecond time scale whereas structural changes in small molecules, bond breakage/formation, isomerisation and electron transfer, span from femtoseconds to nanoseconds. The primary time scale in chemistry is governed by the vibrational period of bonded atoms, with higher Z atoms having longer vibrational periods [1]. For example, the oscillation period in the ground states of H_2 and I_2 are 10 fs and 156 fs, respectively. Structural changes in molecules propagate at the speed of sound, typically 1000 m/s, which corresponds to 100 fs/Å.

The femtosecond time scale became accessible with the advent of ultrafast lasers in the 1980s and spawned the field of femtochemistry. For filming molecular reactions by optical absorption spectroscopy and electron diffraction, the Nobel Prize in Chemistry was awarded to Zewail in 1999 [2, 3]. This work was made possible by the development of chirped-pulse amplification, in which a weak femtosecond optical pulse is stretched before amplification to high energy levels, and then recompressed back to its original pulse duration. Prior to this innovation, for which Gerard Mourou from Ecole Polytechnique in France was awarded the Nobel Prize in Physics in 2019, the pulse energy achievable with ultrashort pulses was severely limited by nonlinear optical processes that would otherwise destroy the gain medium. The ability to amplify femtosecond pulses to high energy levels is critically important for laser/X-ray experiments that often require high pulse energies at specific wavelengths to produce a detectable signal [4].

The time resolution at synchrotrons and XFELs is ultimately limited by the X-ray pulse length, which is 100 ps for synchrotrons and 10–100 fs for XFELs. The longer duration of synchrotron pulses is a consequence of the spread in energy in the electron bunch that arises from random emission of radiation in the bending magnets of the ring. In linear accelerators, the electrons are accelerated without emission and the electron bunch can therefore be very small in space and short in time.

The signal from short pulses is usually not resolved by detectors and the fastest time resolution can only be obtained by the pump–probe method. In a laser/X-ray pump–probe experiment, the system is initiated rapidly and uniformly by a short laser pulse, which triggers a structural or electronic change and a delayed X-ray pulse probes the evolution. By varying the delay, the process is probed or filmed by a series of snapshots that can be stitched together into a movie. The instrumental time resolution is the convolution of the X-ray and laser pulse lengths and their relative jitter. The pump–probe principle is shown in Figure 2.

The present manuscript is organised as follows. First, we briefly describe the European Synchrotron Radiation Facility (ESRF) in Grenoble, where the first picosecond X-ray experiments were performed in 1994. This is followed by a short presentation of the Extremely Bright Source (EBS) upgrade of the ESRF to a nearly diffraction limited source that was completed in January 2020. The pulse intensity and spectral bandwidth of the EBS beam and the potential for new experiments will also be discussed. Then we'll present some unpublished work from early pump probe experiments at ESRF examining the dissociation and recombination dynamics of I_2 in liquid CCl_4 and the dissociation of CO from Myoglobin studied by Laue diffraction that was the first 3D movie of a protein at work. The manuscript will finally mention a few XFEL experiments with femtosecond resolution.
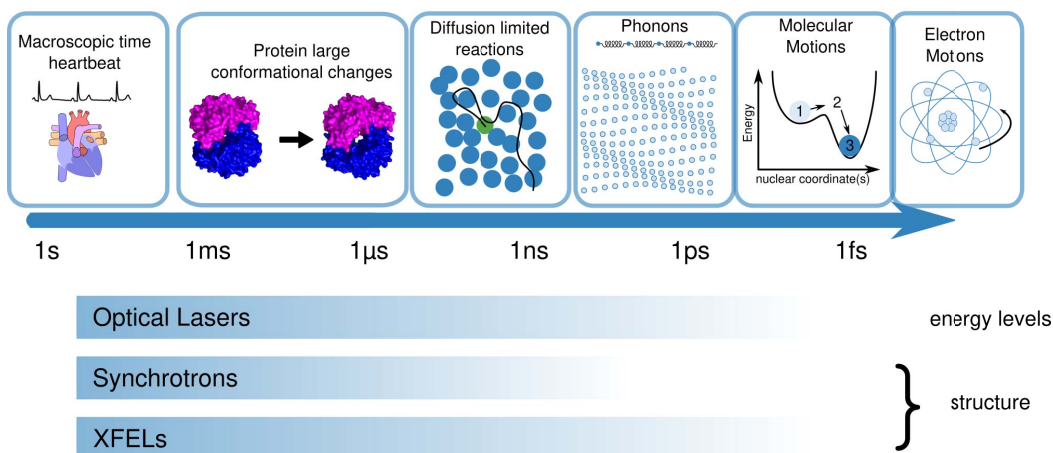
Figure 1. Dynamic process and techniques. On time scales below 1 ms, the time resolution is obtained by pump–probe with optical reaction initiation.
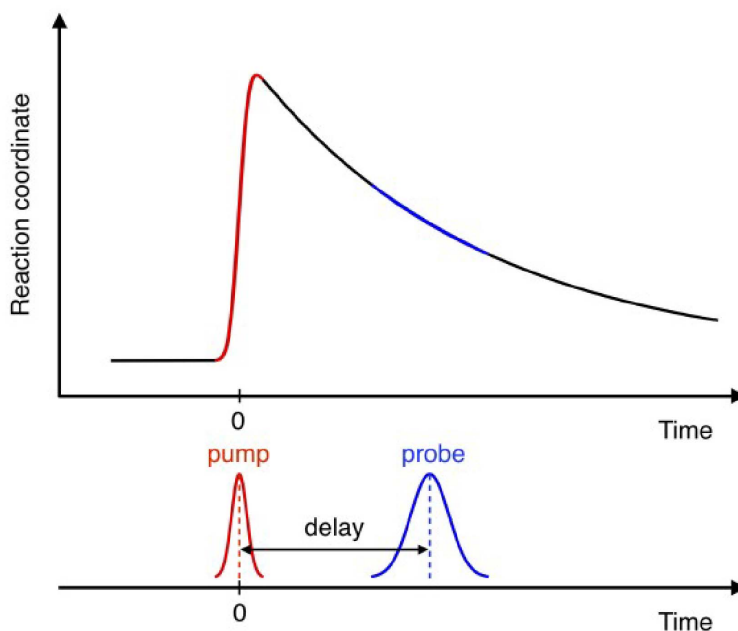

Figure 2. Pump and probe principle. The pump pulse (red) triggers a structural change that is probed by a delayed X-ray pulse (blue). When the sample is refreshed between pulses, the diffraction pattern arising from single pump–probe pairs can be accumulated on an area detector to improve the signal to noise ratio. In femtosecond serial crystallography, the flux is so high that diffraction patterns from single probe pulses can be indexed. The technique is freed from radiation damage since diffraction is faster than radiation damage.

2. Pump probe experiments at ESRF

The European Synchrotron Radiation Facility (ESRF) was the first large synchrotron to produce hard X-rays from undulators. It is a 6.0 GeV ring with a circumference of 844 m. With its sister

Figure 3. European Synchrotron Radiation Facility (ESRF) in Grenoble (2020). The facility is funded by 22 countries, employs 705 people (2021), and has 47 beamlines including collaborating research group beamlines (CRG). The seven-bend-achromat lattice was installed during a 12-month shutdown in 2019 and opened for users in August 2020.

facilities in the USA and Japan, the APS at Argonne and SPring8 near Kyoto, these third-generation synchrotrons have revolutionised X-ray science in fields from nuclear physics to cultural heritage. This is due to the wide energy range, high radiation intensity, coherence and short pulses. The ESRF has 47 beamlines, where 750 experiments are conducted with users per year. Beam time is allocated in peer review competition. The ESRF is shown in Figure 3. The beamlines are highly specialised with unique optics, sample environments and detectors. The facility was upgraded in 2014 with 6 long beamlines with nanometre focusing. The extended experimental hall for these beamlines appears in the photo with the reddish roof.

In spite of the success of third-generation synchrotrons, the large horizontal emittance is an obstacle for making smaller and more coherent beams. The ESRF storage ring was upgraded in 2019 to become a diffraction-limited storage ring, the Extremely Bright Source (EBS). In the EBS design, the maximum curvature in the bending sections in the ring is reduced by the use of 7 closely spaced bending magnets rather than by two strongly deflecting electromagnets in classical designs. The extended bend of the orbit reduces the energy loss to synchrotron radiation making the electron beam more monochromatic, which reduces the spatial dispersion everywhere in the ring. The current of the electron beam is kept constant at 200 mA by frequent top-ups, typically every 10 min at present. The cross section of the electron beam is $76 \times 16 \ \mu m^2$ (H × V) in the insertion device sections (FWHM). The brilliance of the photon source has increased by 30–100 depending on the photon energy. The EBS principle is shown in Figure 4 together with the U17 undulator spectra. The EBS pulse length is unchanged, for the time being at least, at 100 ps (FWHM). For more details the reader is referred to the articles by Pantaleo Raimondi, the ESRF accelerator director, who designed the lattice with his colleagues [5, 6].

As for the technology for pump–probe experiments at synchrotrons, the first issue to consider is that the repetition rate of wavelength tuneable lasers is much lower that the X-ray pulse frequency. The present picosecond laser on beamline ID09 runs at 1 kHz compared to the synchrotron producing 5.7 MHz pulses in the 16-bunch mode. In practice, the X-ray frequency is
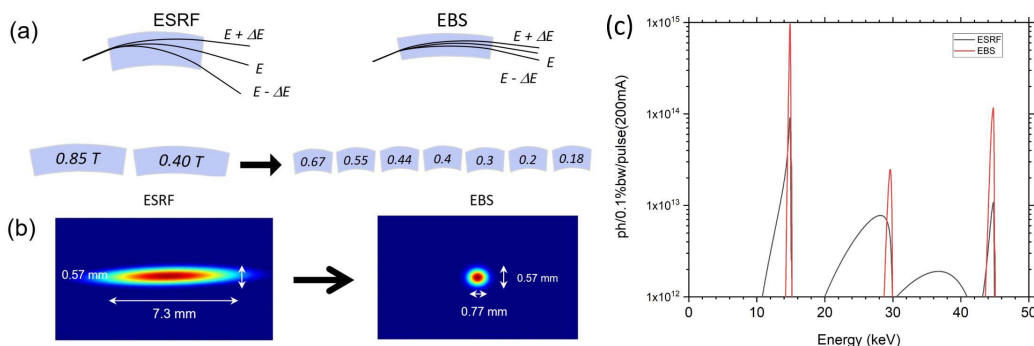
Figure 4. Comparison of the original ESRF and upgraded EBS synchrotron. (a) Dispersion of the electron beam passing through a bending magnet sector. The dispersion is reduced by employing 7 bending magnets rather than by 2 strong ones used in the old design, which results in a 30-fold reduction in horizontal emittance. (b) Beam profile of the EBS and ESRF beam 27 m from the source (U17 undulator @ 15 keV). (c) Spectral intensity of the U17 undulator for the ESRF and EBS. The intensity is measured in a 0.5×0.5 mm^2 slits 27 m from the source to show the gain in intensity in the centre of the beam. Many experiments can be performed without a monochromator, which affords a very significant gain in flux.

lowered by mechanical choppers, which allow to isolate single pulses from special diluted filling modes of the ring. The ID09 choppers reduce the average intensity (ph/s) on the sample by a factor 5700. As a result, it is important to use the intense pink beam ($\sim$100 W) whenever possible. The intensity of the radiation increases with the magnetic field acting on the electrons and to maximise the field, the magnets in the U17 undulator are inside the vacuum of the storage ring. The bunch current is limited to 10 mA/bunch in 4-bunch mode due to the reduction in lifetime at higher currents. The maximum flux from the U17 undulator is 1×10^{10} ph at 15 keV for a 10 mA bunch with fully opened slits. At this setting the relative bandwidth $\delta E/E$ is 4.0% which can be used in small angle scattering experiments. If the slits are set to accept the central cone only, the bandwidth is reduced to 2.0% with 1×10^9 ph/pulse.

One advantage of reducing the pulse frequency to 1 kHz is that a liquid sample can be exchanged between pulses in a flow cell so that irreversible processes can be studied [7]. The lower frequency also protects the sample from the damage of the full beam. In practice, the white beam at ID09 is first chopped by a pre-chopper, the so called heatload chopper, into 36 µs pulses at 1 kHz. These macro pulses are then chopped by a high-speed chopper (HSC) in front of the sample. The rotor in the HSC is a flat triangle with two slits at the tips of one of the three edges. The HSC opens for 265 ns, short enough for isolating a single pulse from the 4-bunch, 16-bunch and hybrid mode. The isolation of a single pulse from the 16-bunch mode is shown in Figure 5. The details of the chopper system are described by Cammarata *et al.* [8].

A typical sample environment for pump–probe liquid experiments is shown in Figure 6. The 1.2 ps laser pulse impinges on the sample 15° above the collimator pipe and the delayed 100 ps X-ray pulse is guided to the sample inside a pipe to reduce air scattering. The diffracted signal is recorded by a CCD detector (Rayonix MX170-HS). As mentioned, the pump-pulse frequency for liquid experiments is 1 kHz, whereas experiments with solid samples run at lower frequencies due to the heatload from the laser. In liquid experiments, the detector is exposed for 1–10 s before readout, accumulating 1000–10000 X-ray pulses in the image. To extract the laser induced change, the experiment is first done without laser or, better, at a negative delay, to keep the average sample temperature constant. After azimuthal integration and scaling of the resulting 1D curves
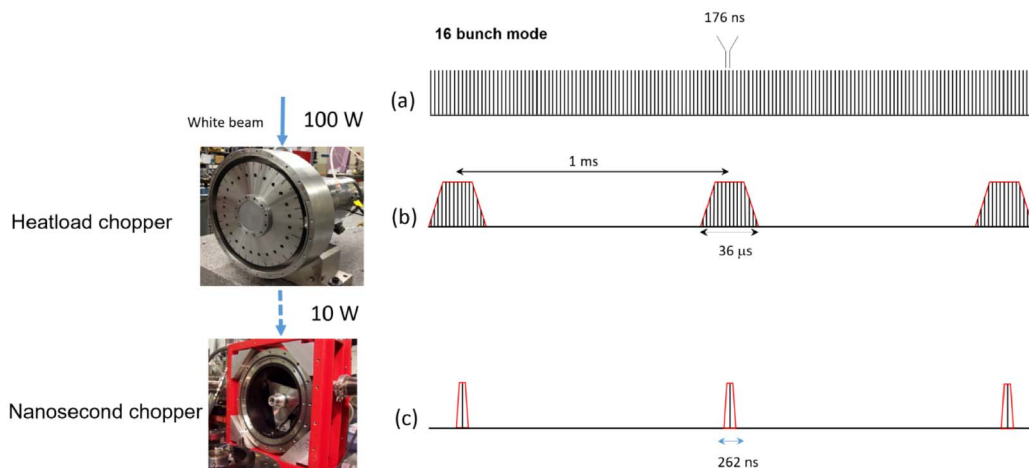
Figure 5. Chopper system on beamline ID09/ESRF. (a) The 16-bunch mode has 176 ns between pulses. (b) To reduce the heat load on the optics, the beam is pre-chopped into 37 μs bursts of pulses at 1 kHz. (c) Single bunches from each burst are isolated by a nanosecond chopper, which transmits a 1 kHz pulse train of ~100 ps pulses.
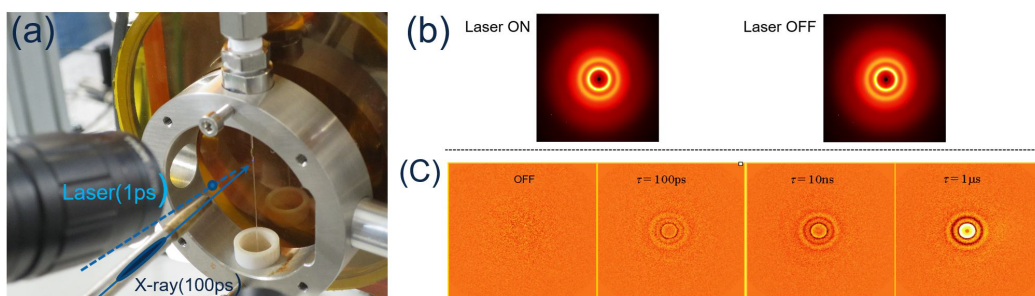

Figure 6. (a) Flow cell used for wide-angle scattering on ID09/ESRF. The liquid solution is injected in a capillary. It is then exposed to a 1.2 ps laser pulse followed by a delayed 100 ps X-ray pulse (illustrated as a 30 mm long needle in the collimator). (b) Scattering patterns from non-excited and excited solutions. The signal from the solute is superimposed on a large solvent background in a ratio of ~1:1000 in most cases. (c) Difference patterns for 3-time delays in the iodine experiment in liquid CCl_4 that is described below.

at high q near the edge of the detector, the difference curves are calculated. Only a fraction of the solutes (or unit cells in a crystal) is excited due to the limited laser penetration or the finite pulse energy that the liquid can tolerate. The shape of the difference curve $dS(q)$ is independent of the degree of excitation since the contribution from non-excited solutes (unit cells) cancels out in the difference. This approximation, however, breaks down in the case of multiphoton absorption or sequential absorption, in which case the laser fluence has to be reduced.

The spectra from ESRF and EBS are compared in Figure 4b. The spectra are measured through a small primary slit 0.5×0.5 mm^2 slit 27 m from the source. The gain in intensity from the EBS is a factor 10. Additionally, the horizontal source size is 60 μmH, a 50% reduction compared with the old synchrotron. The total intensity with fully opened slits is the same for the new and old lattice. The line shape of the EBS fundamental is freed from the low-energy pedestal,

a characteristic synchrotron feature caused by off-axis radiation from the more divergent electron beam. The beam is focused by a Pd coated toroidal mirror to Ø25 μm. The incidence angle is 2.48 mrad and the mirror cut-off 24 keV. Synchrotron beams are very stable unlike XFEL beams for which the position, intensity and spectrum have to be measured pulse-by-pulse and sorted later.

3. Photolysis of small molecules in solution

Historically, the first ultrafast photo triggered reaction was a study of the dissociation & recombination dynamics of I_2 in liquid CCl_4 by *K*. Eisenthal and his colleagues at Bell Labs in 1974 [9]. They found that most of the dissociated I atoms are captured by the liquid cage and that these atoms recombine in 120 ps while heating the solvent. 15% of the dissociated atoms were found to escape the cage and recombine in microseconds via bimolecular diffusion. The potential energy curve for I_2 is shown in Figure 7 for the ground and lower energy states of interest. At large atom–atom separations, the force in the X potential is attractive and drives the atoms closer together towards the potential minimum. At shorter distances, the potential is repulsive. The minimum is the equilibrium bond length of the molecule. A classical and quantum description of diatomic molecules is given by Slater [1]. The paper details the parameters of the Morse potential, the oscillation frequency and amplitude as a function of energy. The energy of the molecule is quantized in discrete vibrational levels, but at ambient temperature, the ground state is essentially 100% occupied. For gas phase I_2, the bond length is 2.666 Å in the ground state. The oscillation frequency is 6.2×10^{12} Hz and the vibrational amplitude 0.05 Å [10]. In Figure 7b, the vibrational relaxation from the dissociation energy to the ground state is simulated assuming a time constant of 100 ps. The amplitude of the oscillation becomes smaller as I_2^* returns to the ground state. The solvent, through collisions, dissipates the excess heat. The Eisenthal experiment was repeated with X-rays at ESRF by Plech *et al.* in [11]. In the I_2:CCl_4 experiment, the heavy solvent molecules slow down the recombination to 140 ps, which can be resolved with 100 ps X-ray pulses from a synchrotron. The first experiment did not resolve the contraction of I_2^* versus time; rather the recombination was inferred from the heat deposition in the solvent from the cooling of $I_2^*(X)$. In a follow-up experiment by Lee and his colleagues in 2013, laser slicing was used to push the time resolution below 100 ps [12]. Slicing takes advantage of the short 1.2 ps laser pulse and the low timing jitter between the pump and probe. By collecting time delays in steps of 10 ps, from -150 to 150 ps, the shape of the $dS(q,t)$ curves could be fitted against a model of the recombination process. The shape of the $dS(q,t)$ curves are consistent with the exponential cooling decay in a Morse Potential.

One important observation from the first iodine studies with X-rays is that the difference curves $dS(q,t)$ have two principal components: the signal from the changes in solute/cage structure, the goal of the experiment, and a thermal signal from the change in temperature, pressure and density of the solvent. The excitation produces molecules in high energy states and the return to the ground state is accompanied by heat dissipation in the solvent. The effect has a unique X-ray signature $dS_s(q)$, which is solvent specific. Since it is impossible to determine two signals from one measurement, the solvent signal has to be measured separately. That can be done by diluting dye molecules that absorb at the wavelength of the experiment. Alternatively, the heat can be generated by exciting the solvent molecules with near infrared light (1000–2000 nm) whereby heat is transferred into vibrational modes, usually via overtones of vibrational modes. Most of the common solvents have been characterised thermally by the dye method by Kjaer and his colleagues in 2013 [13] and the near infrared method was applied by Cammarata and his colleagues [14].
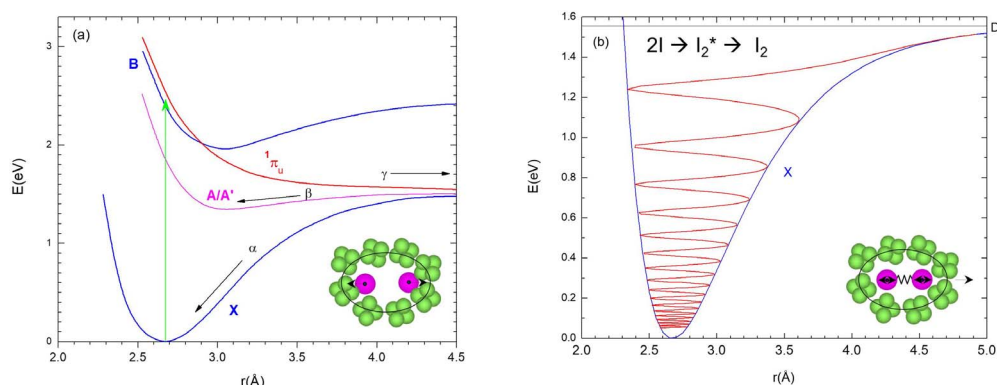
Figure 7. (a) Potential energy of a diatomic molecule illustrated by I_2. Excitation by an ultrashort 530 nm laser pulse excites the molecule vertically into the repulsive B and π states. The dissociated atoms collide with the solvent cage in ~300 fs. Recombination in the cage is the dominant process in CCl_4 with 85% of molecules recombining geminately and 15% escaping the cage. Three pathways have been identified, α and β, and γ corresponding to direct vibrational cooling along the X potential to the ground state, the formation of the A/A' triplet state ($S = 1$) and cage escape. (b) Schematic presentation of X state vibrational cooling. The bond is re-formed at the dissociation energy at 1.52 eV in a large amplitude vibrational state. It relaxes to the ground state while losing energy to the solvent via cage collisions.

When solvent hydrodynamics is included in the analysis, the time dependence of the temperature and density can be determined independently from the low q part of $dS(q)$ which serves as a check of the overall consistency of the model. The temperature and pressure versus time for I_2 in CCl_4 are shown in Figure 8 as an example. The temperature jump at 1 ps is from the first collisions of I atoms with the cage. The temperature is not defined in the early out-of-equilibrium states; it is calculated here from the average energy uptake of the solvent. After 1 ps, the temperature rises from the cooling of $I_2^*(X)$ as illustrated in Figure 7b. After 200 ps, the slope change is due to the recombination of the 2.7 ns A/A' state. After 10 ns, the solvent expands accompanied by a drop in temperature. The expansion proceeds at the speed of sound until the pressure return to ambient in about 1 μs. The pressure versus time profile is shown in Figure 8b. The theory of heat dissipation is described in more detail in the work by Wulff *et al.* [15]. Thus, time-resolved X-ray scattering adds information on the reaction mechanism by being sensitive to all the constituents in the sample.

The structural sensitivity of X-rays to atom–atom distances in molecules is illustrated in Figure 9. The diatomic molecule is exposed to a monochromatic plane wave. The scattering from the two atoms produces spherical secondary waves that interfere. From the intensity profile on the detector, the change in the atom–atom distance can be deduced, even for a random ensemble of molecules. The principle is the same as in Young's two-slit experiment. The averaging over all orientations produces the soft modulated pattern shown in Figure 9b.

Calculating the scattering from isolated gas molecules is the first step in understanding the scattering curves during a chemical transformation. The gas scattering is given by the Debye Function [16]:

$$S(q) = \sum_{i,j} f_i(q) f_j(q) \frac{\sin(q r_{ij})}{q r_{ij}}.$$

Here $f_i(q)$ and $f_j(q)$ are the atomic form factors of atoms i and j and r_{ij} is the distance. The form factors are the sine-Fourier transform of the electron density of the respective atoms. $f(q)$ is
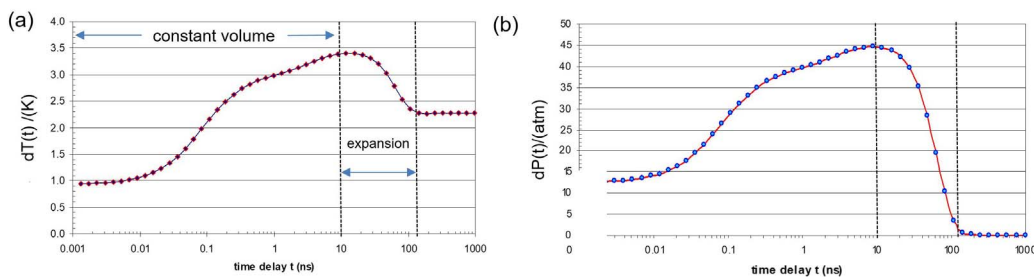
Figure 8. CCl_4 hydrodynamics caused by I_2^* recombination. (a) The solvent temperature versus time. In the time range 0.001 to 0.01 ns, the rise is from the first collisions of trapped I atoms prior to bond formation. From 0.01 to 10 ns, the temperature rises further from the vibrational cooling in the X and A/A' states. The volume is constant and the system adiabatic. In the following time range 10–100 ns, the sample expands due to the pressure gradient caused by the spatial profile of the laser beam. (b) Pressure versus time during recombination.
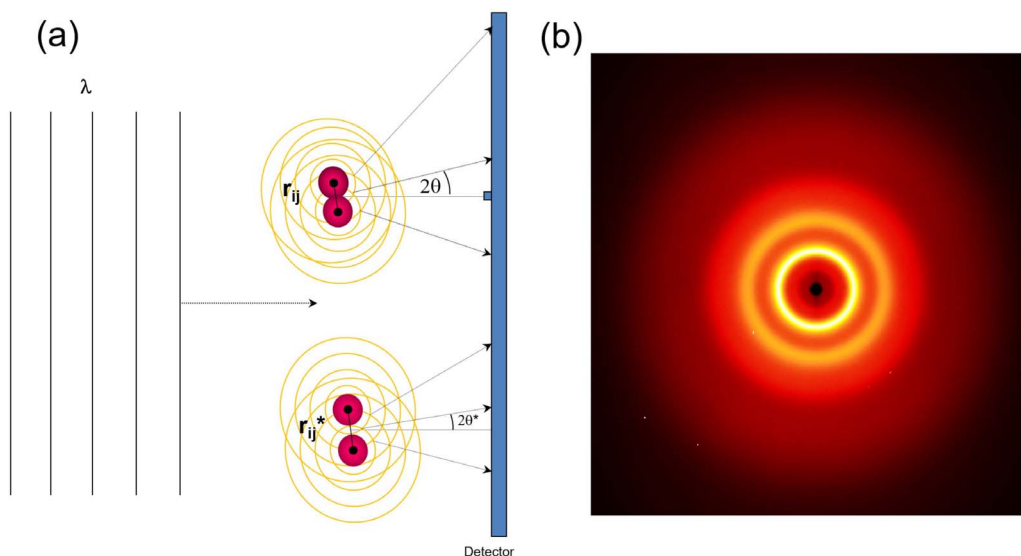

Figure 9. (a) Interference from a diatomic molecule in an X-ray beam. The atoms scatter the radiation isotopically and the interference pattern probes the atom–atom distance. (b) The radiation from randomly oriented molecules produce interference cones on a CCD detector. The dark spot in the centre is the beam stop.

approximately a Gaussian function with a half-width of $2\pi/r$, where r is the atomic radius. The expression applies to an ensemble of gas molecules randomly oriented in space. It should be noted that when X-rays are used to measure positions in a molecule, it is the position of the full electron density that is probed unlike with neutrons that probe the nuclear positions. The Fourier inversion of the X-ray scattering to real space produces peaks and valleys of finite width from the *size* of the atoms. The Debye functions $S(q)$ and $dS(q)$ from structural changes in I_2 are shown in Figure 10 and the experimental curve $dS (q, 460 \text{ ps})$ for I_2 in CCl_4 is shown in Figure 11. The solvent background is ~1000 times greater than the solute signal due to the low solute concentration (mM). It is particularly important to measure $S(q, t)$ well in the high q range
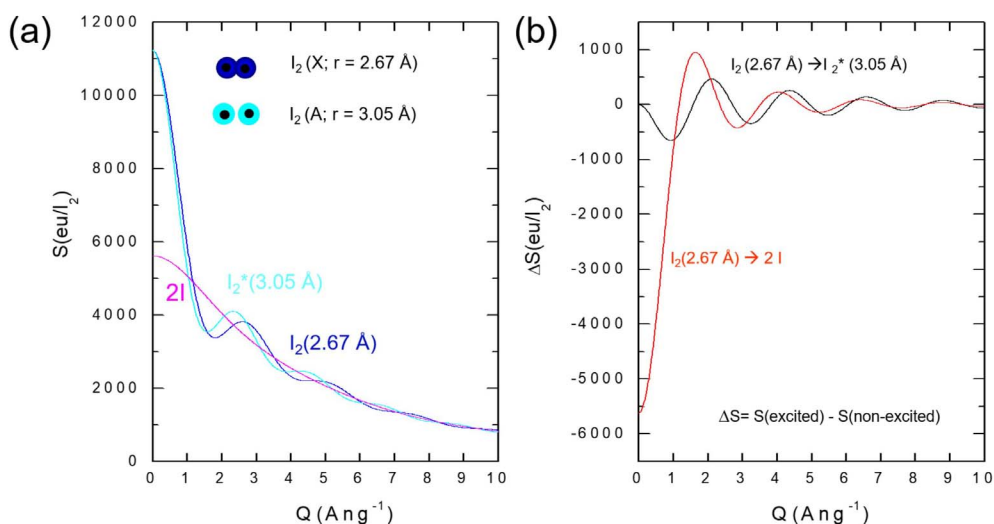
Figure 10. (a) Gas phase scattering from I_2 and I. The forward scattering is proportional to Z_{mol}^2, where Z is the number of electrons in the molecule. In the expanded triplet state I_2^*, the scattering function contracts. (b) Finger printing structural changes. Dissociation has a large negative forward scattering due to the smaller coherent scattering from 2 separated atoms.
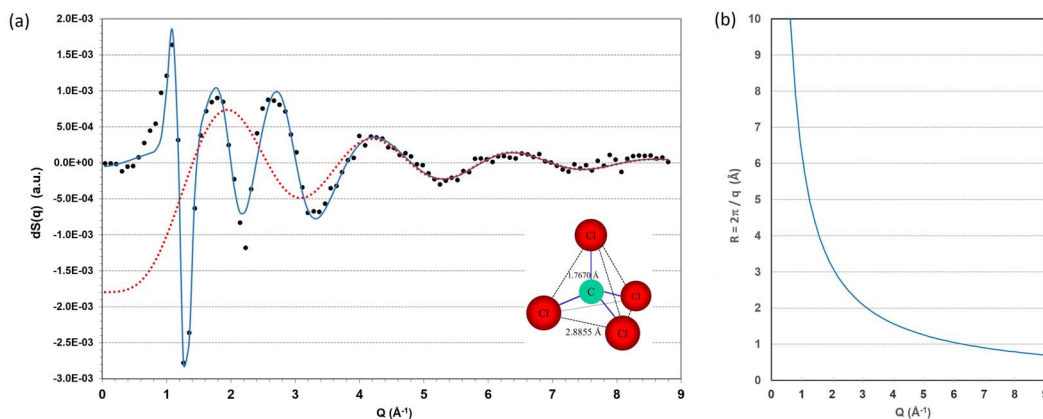

Figure 11. (a) Difference scattering for I_2 in CCl_4 460 ps after laser excitation. The gas component shown in red provides a good fit above $4\,\text{Å}^{-1}$. The experimental difference $dS(q,t)$ has two components: the iodine/cage scattering and the thermal solvent contribution from the change in temperature. (b) Resolution versus Q. Intra molecular changes in iodine dominate the signal for $q > 4\,\text{Å}^{-1}$.

8–$10\,\text{Å}^{-1}$ for the scaling of laser ON and laser OFF images. The scaling is based on the fact that in that range $S(q,t)$ can be calculated by the Debye function for the excited solutes and solvent. Expressed differently, the liquid appears as a collection of gas molecules at high q. In the dS $(q, 460\,\text{ps})$ curve for the I_2:CCl_4 solution, the red curve is the gas phase part as explained in Figure 10b.

In the generalisation of the Debye Equation to a solution, the structure of the liquid solute/solvent mixture is expressed by statistical atom–atom distribution functions $g_{ij}(r)$ that represent the fluctuating structure in a liquid. The $g_{ij}(r)$ functions have two parts: the sharp and well-defined intra molecular part and a broad extra molecular part at larger r that describes the bulk solvent and the solute cage. The scattering is calculated from the $g_{ij}(r)$ functions from MD via:

$$S(q) = \sum_{i,j}^{N,N} f_i(q)f_j(q)\left(N_i N_j \delta_{i,j} + \frac{N_i N_j}{V}\int g_{i,j}(r)e^{iqr}\,dV\right).$$

The expression is a generalisation of the Zernike–Prins formula for monoatomic liquids [17] and molecular liquids as described in the book by Hansen and McDonald [18]. N_i is the number of atoms of kind i, V the volume and $\delta_{ij}(r)$ the Kronecker delta function $\delta_{ii} = 1$, and $\delta_{ij} = 0$ for $i \neq j$. For a time-resolved experiment, the starting solute structures are calculated by density functional theory (DFT) including point charges on the atoms that are important for the solvent interaction. The next step is to perform a MD simulation with the DFT candidate structures for the ground and excited states structures. MD calculations assume thermal equilibrium so only quasi stationary structures can be approximated in this way. MD provides the $g_{ij}(r)$ functions including the cage. The Zernike–Prins equation is then used to calculate the change in scattering $dS(q)$.

A more intuitive presentation of the structural changes is obtained by the sine-Fourier transform:

$$\Delta S[r, t] = \frac{1}{2\pi^2 r}\int_0^\infty dq \frac{1}{\sum_{i\neq j} f_i(q)f_j(q)} q\Delta S(q, t)\sin(qr).$$

The denominator in the integral is the sharpening function which partially corrects for the broadening from atomic form factors that, as mentioned, probe the size of the atoms unlike the g_{ij} functions that measure the positions of the nuclei. The notation $\Delta S[r]$, i.e. with square brackets is to distinguish it from the sister $\Delta S(q)$ from which it is derived. $\Delta S[r]$ is an X-ray biased measure of the change in the radial electron density of an average excited atom. High-Z atoms are amplified in X-ray scattering unlike for neutrons.

The $g_{ij}(r)$ functions for the I_2/CCl_4 solution were calculated by the MD software Moldy using 512 rigid CCl_4 and one I_2 molecule. The $g_{ij}(r)$ functions that probe the cage for $I_2(X)$ are shown in Figure 12(a). The cage radius is given by g(I–Cl) since I is surrounded by Cl atoms in CCl_4. The first peak in g(I–Cl) is at 3.93 Å. The first coordination shell is at 5.10 Å as defined by the first peak in g(I–C).

The change in the cage structure of the reaction products are examined in Figure 11b. The g(I–Cl) distributions for X and A are nearly identical, in position and amplitude, as expected from the bond elongation of ~0.38 Å in the A/A's state. In contrast, the $I_2(X) \rightarrow 2I$ and $I_2(A/A') \rightarrow 2I$ transitions lead to a 27% increase in Cl population around I. The number of I–Cl pairs increases after dissociation as Cl fills the space vacated by I.

The real space change $\Delta S[r]$ is shown in Figure 13 for the gas and solution phase transitions. In the simple gas phase transition $I_2(X) \rightarrow I_2(A/A')$, the bond expands from 2.67 to 3.05 Å. That gives a negative peak for the depletion of the ground state and a positive creation peak. The change in cage structure follows that trend, i.e. the cage radius is slightly larger for A/A'. The gas phase reaction $I_2 \rightarrow 2I$ with I atoms infinitely apart, has a single depletion peak at the $I_2(X)$ bond length. In solution, the entering Cl atom produces a positive peak at 3.9 Å. In summary, time-resolved wide angle scattering with synchrotron and XFEL radiation is a powerful method for structural studies of molecular reactions in solution. The X-rays probe all pairs of atoms and that provides precious information about the structural dynamic. When the X-ray data is taken over a wide q range, the excited solute structures and the hydrodynamics parameters of the solvent medium can be determined from models combining DFT and MD.
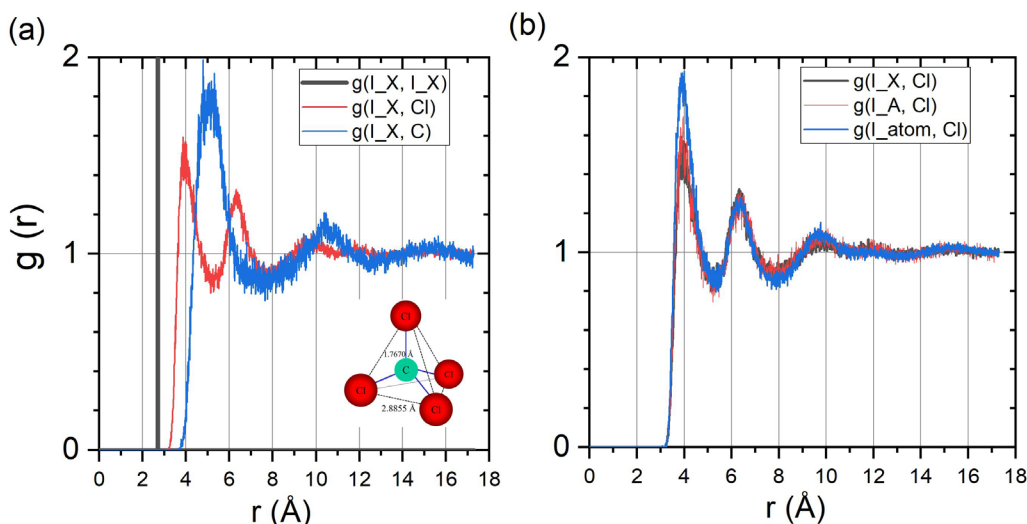
Figure 12. Molecular dynamics of I_2 in CCl_4 with g functions for I_2 and I in the X, A and atomic state. (a) I_2 is in the ground state X. The cage radius is the first peak in g(I–Cl) at 3.93 Å. The first peak in g(I, C) is at 5.10 Å, the distance to the centre of CCl_4. (b) Cage functions for the three states of iodine. For free I atoms, Cl fills the space vacated in the dissociation expressed by the increase of the blue curve at 3.93 Å.
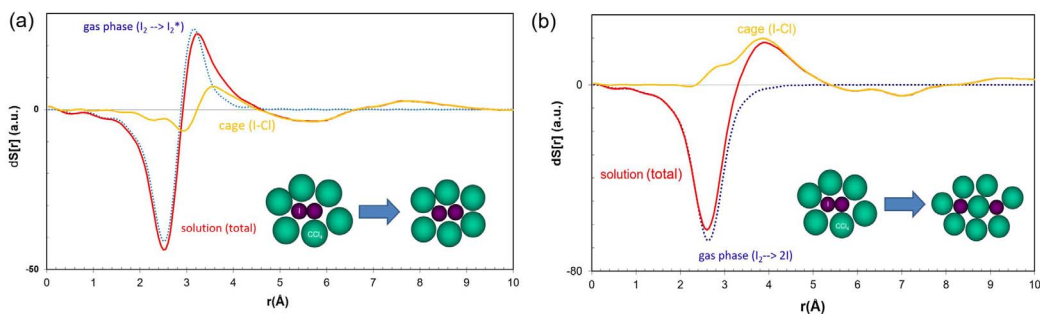

Figure 13. Change in radial distribution function dS[r] probed by X-ray scattering. (a) Signature of bond elongation in the $I_2(X)$ to $I_2(A/A')$ transition. The red curve shows the total difference signal from the A/A' state formation calculated from the MD simulation. The negative peak at ~2.7 Å shows the depletion of ground state I_2 and the positive peak at 3.2 Å, the creation of the A/A' state. The cage component is shown in yellow. (b) Signature of cage escape of I atoms. In this process, the missing I neighbour in I_2 is replaced by Cl.

4. Protein dynamics in solution

Many proteins cannot be crystallised and time-resolved wide-angle scattering in solution offers a way to study large amplitude conformational changes. The low protein concentration (few mM or less) is a challenge and the large size, about a thousand times larger than a small molecule, complicates the analysis. Recent TR-WAXS data from proteins have demonstrated that medium and large-scale changes in some photo sensitive proteins are to be checked against model predicted scattering patterns. The TR-WAXS method for proteins was pioneered by Marco Cammarata and his colleagues on human haemoglobin (Hb), a tetrameric protein with two
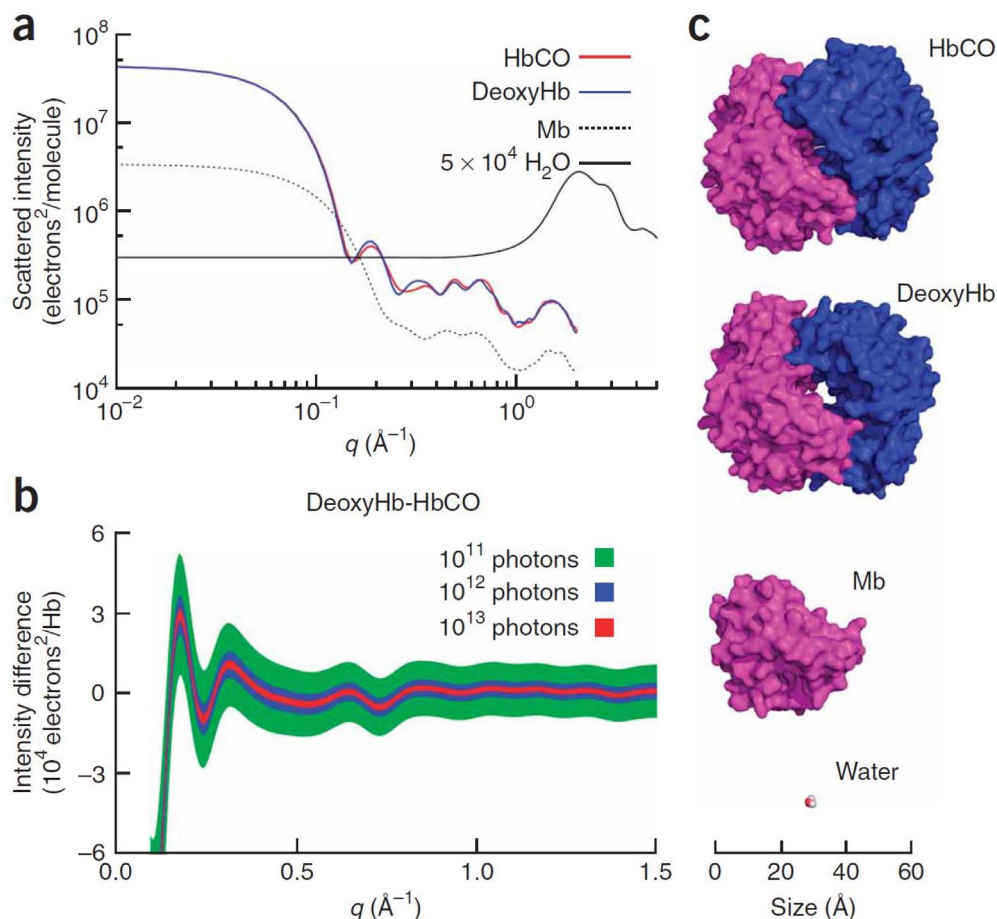
Figure 14. Calculated Debye scattering for haemoglobin (HbCO and Hb), myoglobin (Mb) and water. The calculations were performed with CRYSOL using the crystal structures adapted to the solution phase. The protein signal is much stronger than the water background in the low q limit. (b) Relative change of the protein signal to the water background for the R-to-T transition (HbCO → Hb) for an excited-state concentration of 1 mm. (c) Snapshots of the molecular structures used in the simulations [18].

identical $\alpha\beta$ dimers [19]. HbCO in solution is known to have two quaternary structures, a ligated stable R (relaxed) state and an unligated stable T (tense) state. The tertiary and quaternary changes of HbCO, initiated by a ns green laser pulse, were probed by TR-WAXS [20, 21]. The analysis was using the allosteric kinetic model for Hb. It was found that the R–T transition takes 1–3 µs which is shorter than observed by optical spectroscopy. In Figure 14a the gasphase scattering from the crystal structures of HbCO and Hb (deoxyHb) is shown together with a myoglobin and water molecule. In Figure 14b, the relative change from the transition HbCO → Hb is calculated for a 1 mM concentration. Note the good signal-to-background ratio between 0.1–1 Å^{-1} due to the weak water scattering in that q range. The structure of the proteins and water is shown in Figure 14c. The optically induced tertiary relaxation of myoglobin and the refolding of cytochrome c were also studied with TR-SAXS/WAXS. The advantage of TR-SAXS/WAXS over time-resolved X-ray protein crystallography is that it can probe irreversible reactions and large-scale conformational changes that cannot take place within a crystal [22–24].
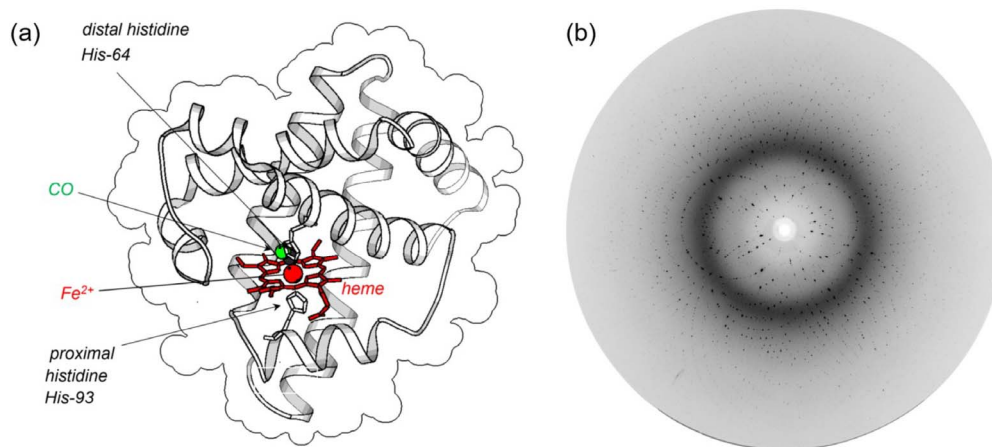
Figure 15. (a) Myoglobin is composed of a single polypeptide chain of 153 amino acids. There are 1270 atoms without hydrogen ($C_{823}N_{222}O_{221}S_3Fe$). MbCO retains its ligand binding functionality in crystals. (b) Laue pattern from a pink beam (0.775 Å, 4% bw, 2×10^9 ph/pulse). 32 pulses are accumulated on the detector (MARCCD 130). The dark ring is from water scattering. The data was analysed to 1.9 Å resolution.

Although the scattering patterns from proteins in solution contain structural information, the information is insufficient to reconstruct the structure in atomic detail. In this respect the use of structures from X-ray crystallography and NMR as a starting point is promising and the development of a more advanced analysis is in progress. For more information on these techniques the reader is referred to the recent articles by Bjorling *et al.* [25] and Ravishankar *et al.* [26].

5. Filming a protein at work by Laue diffraction

Myoglobin (Mb) is a ligand-binding heme protein whose structure was the first to be solved by X-rays in 1958 [27, 28]. Its Fe atom reversibly binds small ligands such as O_2, CO and NO, which is readily photo dissociated from the heme. The structural changes triggered by ligand photolysis was first filmed with near-atomic resolution at the ESRF in 1996 via time-resolved Laue diffraction by Keith Moffat, University of Chicago and Michael Wulff, ESRF and their co-workers [29].

Diffraction images were generated by single, 100 ps X-ray pulses photolysis of MbCO. The structure of MbCO is shown in Figure 15a. A Laue pattern from a monoclinic crystal (P21) with a linear size of 100–200 µm shown in Figure 15b.

The work was done using monoclinic crystals (P21) with a linear size of 100–200 µm as shown in Figure 16a. The packing of the unit cells is shown in Figure 16b for the hexagonal lattice. The latter shows the arrangement of the unit cells and the important space between them that is filled with water. The suspension in water allows the crystalline state to undergo smaller structural changes freed from lattice constraints.

The photolysis of a protein crystal is delicate and should be done without damaging the crystal, while still exciting enough unit cells to give a detectable signal. For example, the absorption gradient of the laser beam in the crystal has to be small to avoid thermal bending and thus broadening of the diffraction spots. The unit cell concentration is high in the monoclinic structure, (49.3 mM), so the laser wavelength has to be chosen judiciously to penetrate the crystal. The MbCO absorption spectrum has three features, the Soret band at 420 nm and two weaker bands
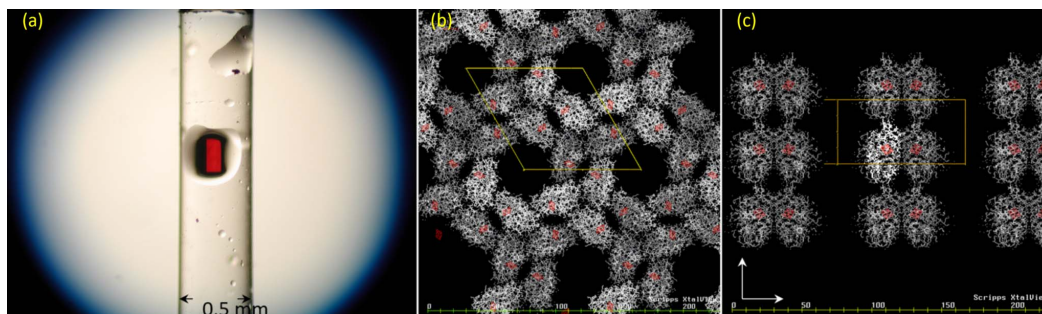
Figure 16. (a) MbCO in the P6 hexagonal lattice (a = b = 91.20 Å, c = 45.87 Å, $\alpha = \beta = 90°$, $\gamma = 120°$). (b) Structure along the c axis. The heme is shown in red. The black areas are water channels. (c) Structure along the a axis.

at 550 and 585 nm, the Q bands α and β. The penetration depth is 1.5 μm on the Soret band and 15 μm on α and β. However, by exciting on the shoulder of the β band at 625 nm, where dissociation still works, the absorption length is 420 μm, a good match to the crystal dimensions in the experiment [30, 31]. The fraction of unit cells photolyzed by a 1 mJ pulse of 0.5 mm diameter was ~20–30%.

The crystals were mounted in capillaries in a CO atmosphere and 16–32 images from single pulses were accumulated on the detector before readout. The crystals were rotated in steps of 3°, from 0–180° to fully sample reciprocal space. In some cases, the crystals would be damaged after some time, then replaced and the data merged later.

The diffraction pattern is sensitive to changes inside the unit cells. When the non-excited starting structure is known from the PDB data base, the measured intensity changes $dI(hkl)$ allow to determine the change in electron density via the Fourier Difference Method [31]. The first experiment used the spectrum from a wiggler (W70) covering 7–28 keV. The wiggler was replaced in 2000 by the narrow-band undulator U17 which increased the SNR due to a much lower diffuse background from water in the protein. A second spin off of the narrow band is the lower number of spatial overlaps in the images from the well-defined relation between the scattering angle and the d-spacing (Bragg's law) provided by the narrow 5% bandwidth spectrum at 15 keV.

From the measurements of 50,000 intensity changes $\Delta I(hkl)$, the Fourier difference maps were derived as shown in Figure 17. The difference density is superimposed on the CO ligated initial structure in white: red volumes are due to loss of density, blue is from a gain. CO is seen to move to the solvent via 2 interstitial cavities. Initially, it is trapped in a small cavity next to Fe for 5 ns. The CO hole is partially filled by a shift in position of the distant His-64 that blocks geminate recombination. The new CO position is also pushing the Ile-107 residue slightly. Note the tilt of the heme plane and the Fe motion out of the plane. The doming is from the change in coordination from 6 to 5 of Fe after dissociation. Note that red and blue volumes are side-by-side consistent with small rigid translocations. In the 30 ns map, the first cavity is empty and CO is not resolved. In the 300 ns map, CO reappears on the proximal side in a cavity, which is known from studies of Xe gas pockets in myoglobin under pressure. The Fe heme doming persists in the absence of the Fe–CO bond. CO diffuses to the solvent and returns to Fe via random diffusive motion on the ms time scale.

The first Laue work on sperm whale myoglobin was followed by studies of on mutants lead by Anfinrud [32] and Brunori [33]. As the CO is on the distal side of the heme at early time delays, the protein function is strongly influenced by the amino acid side chains around that site. The L29F mutant of MbCO, where leucine Leu29 is substituted by phenylalanine, exhibits 1000 time faster dynamics [32].
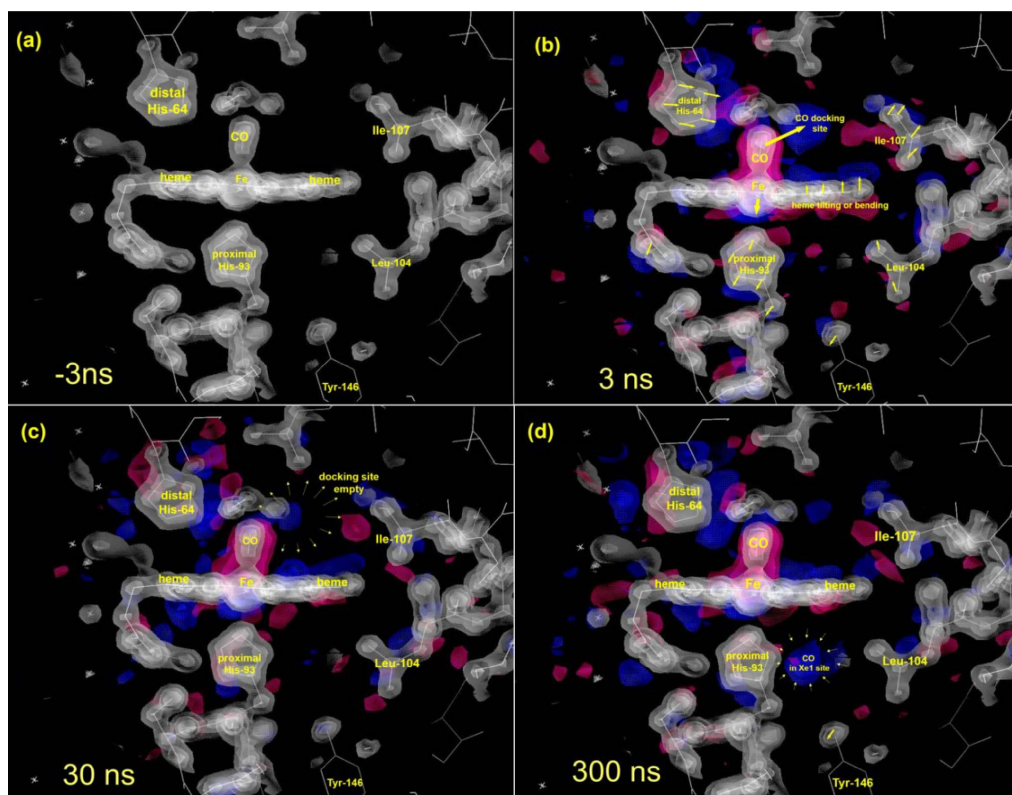
Figure 17. 3D maps of the dissociation of CO from the Fe binding site in sperm whale Myoglobin MbCO. The dissociation is triggered by a 2.3 ns laser pulse at 620 nm. (a) Initial electron density of MbCO near the heme. The electron density is contoured in white at 3, 5 and 7σ. The map is the 2MGK model of sperm whale MbCO at 1.7 Å resolution. (b) Fourier difference maps taken 3 ns after dissociation by single pulse Laue diffraction. The difference is superimposed on the initial state. Red represent loss of density, blue gain in density. CO is captured in the "docking site" on the distal side of the heme. Fe has moved 0.2 Å out of the heme plane in response to the change in coordination from 6 to 5. Note how the distal and proximal histidine move in response to the new CO position. That structural change blocks CO geminate recombination to Fe. (c) At 30 ns the docking site population is decreasing. (d) After 300 ns, CO is accumulating in a pocket on the proximal side from where it diffuses into the solvent. After 1 ms, CO returns to the binding site. That pathway is not observed due the loss of synchronization in the reverse reaction. The maps are rendered with the software O7.0 (Alwen Jones, Uppsala University).

6. XFEL experiments

The Linear Coherent Light Source (LCLS) at SLAC in Stanford was the first hard X-ray FEL facility to open in 2009. The LCLS was followed by SACLA at SPring8 in Japan in 2011, SwissFEL in Villigen (CH) in 2016 and the European EuXFEL in Schenefeld (D) in 2017. In XFELs bunches of electrons are accelerated to 5–15 GeV in a linear accelerator and injected into long undulators. After a certain point in the undulator, the X-ray field induces a density modulation in the bunch, the SASE effect, which amplifies the intensity by orders of magnitude. The electrons in a micro

bunch emit in phase as super electrons. The intensity is then proportional to N_e^2 (micro bunch electrons) × N_p^2 (periods). The energy range is currently limited to 1–16 keV but higher energies will become available at the EuXFEL in the near future. For a review of the SASE principle, the reader is referred to the article by Margaritondo *et al.* [34]. XFEL pulses are 10^3 to 10^4 times shorter than synchrotron pulses, i.e. 10–100 fs, and the intensity can reach 1×10^{12} photons/pulse in a 0.1% BW at 12 keV. The beam is less stable due to the stochastic nature of SASE and it is important to record the beam parameters, the timing jitter in particular, for every pulse. To exploit the short XFEL pulses, the laser/X-ray delay has to be sorted and averaged after the experiment.

Femtosecond pulses are perfect for filming bond breakage and bond formation in chemical reactions, isomerization, electron transfer reactions and coherent wave packet motion etc. Diffraction patterns from micro and nano-sized proteins can be acquired with single XFEL pulses. The number of diffraction spots is large enough for indexing, i.e. determining the orientation of randomly oriented crystals, and the pulse is so short that the diffraction can be recorded before the crystal is destroyed by the Coulomb explosion as described by Neutze *et al.* [35]. The term "diffraction before destruction" is the principle behind Serial Femtosecond Crystallography (SFX). The crystals are injected in the XFEL beam from a jet and thousands to millions of crystals are exposed randomly. By merging the scaled intensity data from thousands of images, the structure can be determined. There are two major advantages of SFX: very small crystals are easier to produce and the structure can be determined at room temperature rather than at cryogenic temperature, where the mobility of the protein is greatly reduced. The reader is referred to the review by Chapman *et al.* for more details [36]. The SFX technique is applicable to pump–probe work on light sensitive proteins as well. Schlichting and her co-workers studied the helix dynamic following photo dissociation of CO from myoglobin MbCO at the LCLS using SFX at 6.8 keV with a resolution of 1.8 Å [37]. The study revealed that the C, F and H helices move away from the heme whereas the E and A helices move towards it in less than 500 fs, confirming the results previously obtained with TR-WAXS measurements at the LCLS on MbCO [38].

One of the first scattering experiments probing a femtosecond chemical reaction in solution was performed by Hyotcherl Ihee from KAIST in Korea in collaboration with Shin-ichi Adachi, KEK, using the SACLA XFEL at SPring8 [39]. They studied the formation of a gold trimer $[Au(CN)_2^-]_3$. In the ground state, the Au atoms in three molecules are weakly bonded by van der Waals interactions. Upon photo activation, an Au electron is excited to a bonding orbital producing a covalent Au–Au bond with a linear geometry with a lifetime of 500 fs. The Au bonds shorten in a second 1.6 ps step. Finally this linear conformation combines with a free $Au(CN)_2^-$ in 3 ns to form a tetramer. The reaction is shown in Figure 18.

The first X-ray spectroscopy experiment from an XFEL was reported by Henrik Lemke and Marco Cammarata and their co-workers in 2013 [40]. They performed a XANES study of the spin-cross-over complex $[Fe(bpy)_3]Cl_2$ in a 50 mM aqueous solution using 100 fs pulses from the LCLS. The position of the Fe absorption edge depends on the Fe–N distance from which they deduce that the switch from the low-spin (LS) to the high-spin (HS) state takes 160 fs. The HS state subsequently decays to the LS state in 650 ps. The experiment was done with fluorescence detection and the XFEL white beam was monochromatized with a diamond monochromator. The K-edge was scanned over 45 eV, the spectral width of the white beam. The main challenge was timing drifts, which could be up to 100 fs per hour. That problem was later solved by time stamping the X-ray pulse followed by sorting the actual delay [41], which allows to exploit the full potential of the short XFEL pulses.

In spite of the high intensity and short pulse from XFELs, synchrotrons will remain important for slower dynamics, from 100 ps to seconds, due to the higher beam stability, wider energy range and easier accessibility. It is also important that users have enough time to get to know the beamline and optimise the experimental parameters.
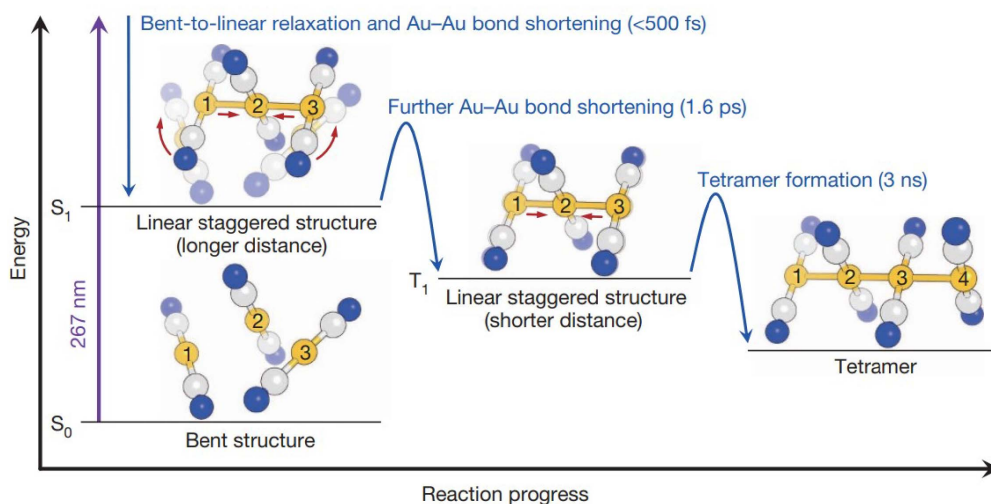
Figure 18. Pioneering solution phase TR-WAXS experiment from an XFEL by the Ihee and Adachi groups. The formation of a covalent bond between the three Au atoms in $[Au(CN)_2^-]_3$ is monitored by time-resolved solution scattering with 100 fs pulses at 15 keV with 1×10^{12} ph/pulse in a 0.6% BW [32].

Table 1. Beam parameters for a synchrotron and XFEL beamline (ID09/ESRF versus FXE/EuXFEL)

Parameter	ID09/EBS	FXE/EuXFEL
Pulse length (ps)	100	0.05
Pulse intensity (ph)	1×10^9	1×10^{12}
Pulses per second	1000	10 (27000)
Energy range (keV)	7–24 keV	6–18 keV
Focus (μm)	25	10
Intensity per second	1×10^{12}	1×10^{13}

The beam parameters for a synchrotron and XFEL beam are shown in Table 1 for ID09 at ESRF and FXE at EuXFEL. The pulse structure at EuXFEL is a 10 Hz macro pulse with each macro pulse having up to 2700 sub pulses that are separated by 220 ns. The large Pixel Detector at EuXFEL and the excitation laser can synchronise to this time structure. It is challenging however, to exchange the samples in the 220 ns dark period between pulses in the macro-pulse train which is often needed since the sample might be destroyed by the pulses.

Acknowledgements

References

[1] N. B. Slater, "Classical motion under a morse potential", *Nature* **180** (1957), p. 1352-1353.

[2] A. H. Zewail, "The birth of molecules", *Sci. Am.* **263** (1990), p. 76-82.

[3] A. H. Zewail, "Filming the invisible in 4-D", *Sci. Am.* **303** (2010), p. 75-81.

[4] G. A. Mourou, D. Umstadter, "Extreme light", *Sci. Am.* **286** (2002), p. 80-86.

[5] P. Raimondi, "The ESRF low emittance upgrade", in *IPAC 2016 – Proc. 7th Int. Part. Accel. Conf.*, CERN, Geneva, 2016, https://accelconf.web.cern.ch/IPAC2016/papers/wexa01.pdf, p. 2023-2027.

[6] P. Raimondi, "ESRF-EBS: The extremely brilliant source project", *Synchrotron Radiat. News* **29** (2016), p. 8-15.

[7] A. Plech, V. Kotaidis, M. Lorenc, J. Boneberg, "Femtosecond laser near-field ablation from gold nanoparticles", *Nat. Phys.* **2** (2006), p. 44-47.

[8] M. Cammarata, L. Eybert, F. Ewald, W. Reichenbach, M. Wulff, P. Anfinrud, F. Schotte, A. Plech, Q. Kong, M. Lorenc, B. Lindenau, J. Räbiger, S. Polachowski, "Chopper system for time resolved experiments with synchrotron radiation", *Rev. Sci. Instrum.* **80** (2009), article no. 015101.

[9] T. J. Chuang, G. W. Hoffman, K. B. Eisenthal, "Picosecond studies of the cage effect and collision induced predissociation of iodine in liquids", *Chem. Phys. Lett.* **25** (1974), p. 201-205.

[10] E. J. Baran, "Mean amplitudes of vibration of the halogen molecules", *Z. Naturforsch. A* **58** (2003), p. 36-38.

[11] A. Plech, M. Wulff, S. Bratos, F. Mirloup, R. Vuilleumier, F. Schotte, P. A. Anfinrud, "Visualizing chemical reactions in solution by picosecond X-ray diffraction", *Phys. Rev. Lett.* **92** (2004), article no. 125505.

[12] J. H. Lee, M. Wulff, S. Bratos, J. Petersen, L. Guerin, J. C. Leicknam, M. Cammarata, Q. Kong, J. Kim, K. B. Møller, H. Ihee, "Filming the birth of molecules and accompanying solvent rearrangement", *J. Am. Chem. Soc.* **135** (2013), p. 3255-3261.

[13] K. S. Kjær, T. B. Van Driel, J. Kehres, K. Haldrup, D. Khakhulin, K. Bechgaard, M. Cammarata, M. Wulff, T. J. Sørensen, M. M. Nielsen, "Introducing a standard method for experimental determination of the solvent response in laser pump, X-ray probe time-resolved wide-angle X-ray scattering experiments on systems in solution", *Phys. Chem. Chem. Phys.* **15** (2013), p. 15003-15016.

[14] M. Cammarata, M. Lorenc, T. K. Kim, J. H. Lee, Q. Y. Kong, E. Pontecorvo, M. Lo Russo, G. Schiró, A. Cupane, M. Wulff, H. Ihee, "Impulsive solvent heating probed by picosecond X-ray diffraction", *J. Chem. Phys.* **124** (2006), article no. 124504.

[15] M. Wulff, S. Bratos, A. Plech, R. Vuilleumier, F. Mirloup, M. Lorenc, Q. Kong, H. Ihee, "Recombination of photodissociated iodine: A time-resolved X-ray-diffraction study", *J. Chem. Phys.* **124** (2006), article no. 034501.

[16] B. E. Warren, *X-ray Diffraction*, Dover Publications, New York, 1990.

[17] F. Zernike, J. A. Prins, "Die Beugung von Röntgenstrahlen in Flüssigkeiten als Effekt der Molekülanordnung", *Z. Phys.* **41** (1927), p. 184-194.

[18] J.-P. Hansen, I. R. McDonald, *Theory of Simple Liquids: with Applications to Soft Matter*, Academic Press, 2013.

[19] M. Cammarata, M. Levantino, F. Schotte, P. A. Anfinrud, F. Ewald, J. Choi, A. Cupane, M. Wulff, H. Ihee, "Tracking the structural dynamics of proteins in solution using time-resolved wide-angle X-ray scattering", *Nat. Methods* **5** (2008), p. 881-886.

[20] M. Cammarata, M. Levantino, M. Wulff, A. Cupane, "Unveiling the timescale of the R-T transition in human hemoglobin", *J. Mol. Biol.* **400** (2010), p. 951-962.

[21] M. Levantino, A. Spilotros, M. Cammarata, G. Schiro, C. Ardiccioni, B. Vallone, M. Brunori, A. Cupane, "The Monod–Wyman–Changeux allosteric model accounts for the quaternary transition dynamics in wild type and a recombinant mutant human hemoglobin", *Proc. Natl. Acad. Sci. USA* **109** (2012), p. 14894-14899.

[22] M. Levantino, B. A. Yorke, D. C. F. Monteiro, M. Cammarata, A. R. Pearson, "Using synchrotrons and XFELs for time-resolved X-ray crystallography and solution scattering experiments on biomolecules", *Curr. Opin. Struct. Biol.* **35** (2015), p. 41-48.

[23] I. Josts, S. Niebling, Y. Gao, M. Levantino, H. Tidow, D. Monteiro, "Photocage-initiated time-resolved solution X-ray scattering investigation of protein dimerization", *IUCrJ* **5** (2018), p. 667-672.

[24] T. W. Kim, S. J. Lee, J. Jo, J. G. Kim, H. Ki, C. W. Kim, K. H. Cho, J. Choi, J. H. Lee, M. Wulff, Y. M. Rhee, H. Ihee, "Protein folding from heterogeneous unfolded state revealed by time-resolved X-ray solution scattering", *Proc. Natl. Acad. Sci. USA* **117** (2020), p. 14996-15005.

[25] A. Björling, O. Berntsson, H. Lehtivuori, H. Takala, A. J. Hughes, M. Panman, M. Hoernke, S. Niebling, L. Henry, R. Henning, I. Kosheleva, V. Chukharev, N. V. Tkachenko, A. Menzel, G. Newby, D. Khakhulin, M. Wulff, J. A. Ihalainen, S. Westenhoff, "Structural photoactivation of a full-length bacterial phytochrome", *Sci. Adv.* **2** (2016), article no. e1600920.

[26] H. Ravishankar, M. N. Pedersen, M. Eklund, A. Sitsel, C. Li, A. Duelli, M. Levantino, M. Wulff, A. Barth, C. Olesen, P. Nissen, M. Andersson, "Tracking Ca 2+ ATPase intermediates in real time by X-ray solution scattering", *Sci. Adv.* **6** (2020), article no. eaaz0981.

[27] J. C. Kendrew, G. Bodo, H. M. Dintzis, R. G. Parrish, H. Wyckoff, D. C. Phillips, "A three-dimensional model of the myoglobin molecule obtained by X-ray analysis", *Nature* **181** (1958), p. 662-666.

[28] J. C. Brooks-Bartlett, E. F. Garman, "The nobel science: One hundred years of crystallography", *Interdisc. Sci. Rev.* **40** (2015), p. 244-264.

[29] V. Srajer, T.-Y. Teng, T. Ursby, C. Pradervand, Z. Ren, S.-I. Adachi, W. Schildkamp, D. Bourgeois, M. Wulff, K. Moffat, "Photolysis of the carbon monoxide complex of myoglobin: Nanosecond time-resolved crystallography", *Science* **274** (1996), p. 1726-1729.

[30] E. Antonini, M. Brunori, *Hemoglobin and Myoglobin in their Reactions with Ligands*, North-Holl. Publ. Co., Amsterdam, Netherlands, 1972.

[31] J. R. Helliwell, *Macromolecular Crystallography with Synchrotron Radiation*, Cambridge University Press, Cambridge, 1992.

[32] F. Schotte, M. Lim, T. A. Jackson, A. V. Smirnov, J. Soman, J. S. Olson, G. N. Phillips, M. Wulff, P. A. Anfinrud, "Watching a protein as it functions with 150-ps time-resolved X-ray crystallography", *Science* **300** (2003), p. 1944-1947.

[33] D. Bourgeois, B. Vallone, F. Schotte, A. Arcovito, A. E. Miele, G. Sciara, M. Wulff, P. Anfinrud, M. Brunori, "Complex landscape of protein structural dynamics unveiled by nanosecond Laue crystallography", *Proc. Natl. Acad. Sci. USA* **100** (2003), p. 8704-8709.

[34] G. Margaritondo, P. Rebernik Ribic, "A simplified description of X-ray free-electron lasers", *J. Synchrotron Radiat.* **18** (2011), p. 101-108.

[35] R. Neutzo, R. Wouts, D. Van Der Spoel, E. Weckert, J. Hajdu, "Potential for biomolecular imaging with femtosecond X-ray pulses", *Nature* **406** (2000), p. 752-757.

[36] H. N. Chapman, P. Fromme, A. Barty, T. A. White, R. A. Kirian, A. Aquila, M. S. Hunter, J. Schulz, D. P. DePonte, U. Weierstall, R. B. Doak, F. R. N. C. Maia, A. V. Martin, I. Schlichting, L. Lomb, N. Coppola, R. L. Shoeman, S. W. Epp, R. Hartmann, D. Rolles, A. Rudenko, L. Foucar, N. Kimmel, G. Weidenspointner, P. Holl, M. Liang, M. Barthelmess, C. Caleman, S. Boutet, M. J. Bogan, J. Krzywinski, C. Bostedt, S. Bajt, L. Gumprecht, B. Rudek, B. Erk, C. Schmidt, A. Hömke, C. Reich, D. Pietschner, L. Strüder, G. Hauser, H. Gorke, J. Ullrich, S. Herrmann, G. Schaller, F. Schopper, H. Soltau, K.-U. Kühnel, M. Messerschmidt, J. D. Bozek, S. P. Hau-Riege, M. Frank, C. Y. Hampton, R. G. Sierra, D. Starodub, G. J. Williams, J. Hajdu, N. Timneanu, M. M. Seibert, J. Andreasson, A. Rocker, O. Jönsson, M. Svenda, S. Stern, K. Nass, R. Andritschke, C.-D. Schröter, F. Krasniqi, M. Bott, K. E. Schmidt, X. Wang, I. Grotjohann, J. M. Holton, T. R. M. Barends, R. Neutze, S. Marchesini, R. Fromme, S. Schorb, D. Rupp, M. Adolph, T. Gorkhover, I. Andersson, H. Hirsemann, G. Potdevin, H. Graafsma, B. Nilsson, J. C. H. Spence, "Femtosecond X-ray protein nanocrystallography", *Nature* **470** (2011), p. 73-77.

[37] T. R. M. Barends, L. Foucar, A. Ardevol, K. Nass, A. Aquila, S. Botha, R. B. Doak, K. Falahati, E. Hartmann, M. Hilpert, M. Heinz, M. C. Hoffmann, J. Kofinger, J. E. Koglin, G. Kovacsova, M. Liang, D. Milathianaki, H. T. Lemke, J. Reinstein, C. M. Roome, R. L. Shoeman, G. J. Williams, I. Burghardt, G. Hummer, S. Boutet, I. Schlichting, "Direct observation of ultrafast collective motions in CO myoglobin upon ligand dissociation", *Science* **350** (2015), p. 445-450.

[38] M. Levantino, G. Schirò, H. T. Lemke, G. Cottone, J. M. Glownia, D. Zhu, M. Chollet, H. Ihee, A. Cupane, M. Cammarata, "Ultrafast myoglobin structural dynamics observed with an X-ray free-electron laser", *Nat. Commun.* **6** (2015), article no. 6772.

[39] K. H. Kim, J. G. Kim, S. Nozawa, T. Sato, K. Y. Oang, T. W. Kim, H. Ki, J. Jo, S. Park, C. Song, T. Sato, K. Ogawa, T. Togashi, K. Tono, M. Yabashi, T. Ishikawa, J. Kim, R. Ryoo, J. Kim, H. Ihee, S. I. Adachi, "Direct observation of bond formation in solution with femtosecond X-ray scattering", *Nature* **518** (2015), p. 385-389.

[40] H. T. Lemke, C. Bressler, L. X. Chen, D. M. Fritz, K. J. Gaffney, A. Galler, W. Gawelda, K. Haldrup, R. W. Hartsock, H. Ihee, J. Kim, K. H. Kim, J. H. Lee, M. M. Nielsen, A. B. Stickrath, W. Zhang, D. Zhu, M. Cammarata, "Femtosecond X-ray absorption spectroscopy at a hard X-ray free electron laser: Application to spin crossover dynamics", *J. Phys. Chem. A* **117** (2013), p. 735-740.

[41] M. Harmand, R. Coffee, M. R. Bionta, M. Chollet, D. French, D. Zhu, D. M. Fritz, H. T. Lemke, N. Medvedev, B. Ziaja, S. Toleikis, M. Cammarata, "Achieving few-femtosecond time-sorting at hard X-ray free-electron lasers", *Nat. Photonics* **7** (2013), p. 215-218.